

# Tuning of Photoluminescence and Local Structures of Substituted Cations in $x\text{Sr}_2\text{Ca}(\text{PO}_4)_2-(1-x)\text{Ca}_{10}\text{Li}(\text{PO}_4)_7:\text{Eu}^{2+}$ Phosphors

Mingyue Chen,<sup>†</sup> Zhiguo Xia,<sup>\*,†</sup> Maxim S. Molokeyev,<sup>‡,⊥</sup> Ting Wang,<sup>#</sup> and Quanlin Liu<sup>†</sup>

<sup>†</sup>The Beijing Municipal Key Laboratory of New Energy Materials and Technologies, School of Materials Sciences and Engineering, University of Science and Technology Beijing, Beijing 100083, China

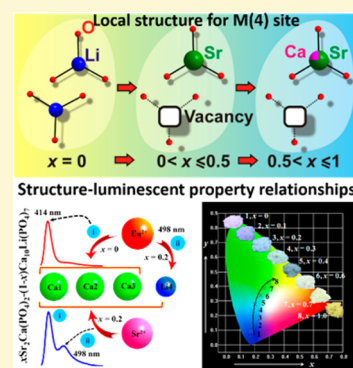
<sup>‡</sup>Laboratory of Crystal Physics, Kirensky Institute of Physics, Federal Research Center KSC SB RAS, Krasnoyarsk 660036, Russia

<sup>⊥</sup>Department of Physics, Far Eastern State Transport University, Khabarovsk, 680021 Russia

<sup>#</sup>State Key Laboratory of Tribology, Tsinghua University, Beijing 100084, China

## Supporting Information

**ABSTRACT:** Local structure modification in solid solution is an essential part of photoluminescence tuning of rare earth doped solid state phosphors. Herein we report a new solid solution phosphor of  $\text{Eu}^{2+}$ -doped  $x\text{Sr}_2\text{Ca}(\text{PO}_4)_2-(1-x)\text{Ca}_{10}\text{Li}(\text{PO}_4)_7$  ( $0 \leq x \leq 1$ ), which share the same  $\beta\text{-Ca}_3(\text{PO}_4)_2$  type structure in the full composition range. Depending on the  $x$  parameter variation in  $x\text{Sr}_2\text{Ca}(\text{PO}_4)_2-(1-x)\text{Ca}_{10}\text{Li}(\text{PO}_4)_7:\text{Eu}^{2+}$ , the vacancies generated in the M(4) site enable the nonlinear variation of cell parameters and volume, and this increases the magnitude of M(4) $\text{O}_6$  polyhedra distortion. The local structure modulation around the  $\text{Eu}^{2+}$  ions causes different luminescent behaviors of the two-peak emission and induces the photoluminescence tuning. The shift of the emission peaks in the solid solution phosphors with different compositions has been discussed. It remains invariable at  $x \leq 0.5$ , but the red-shift is observed at  $x > 0.5$  which is attributed to combined effect of the crystal field splitting, Stokes shift, and energy transfer between  $\text{Eu}^{2+}$  ions. The temperature-dependent luminescence measurements are also performed, and it is shown that the photoionization process is responsible for the quenching effect.



## INTRODUCTION

Phosphor-converted light emitting diodes (*pc*-LEDs) are recognized as the main method for solid-state lighting applications. To target *pc*-LEDs with specific photoluminescence properties, phosphors with different host systems corresponding to various emission characters have been investigated.<sup>1–5</sup> Among them, phosphate phosphors, especially with  $\beta\text{-Ca}_3(\text{PO}_4)_2$ -type structure, are of considerable interest because of their versatile structural types and the substitution-induced different local structures, as well as the tunable photoluminescence behaviors after rare earth doping.<sup>6,7</sup> Herein,  $\beta\text{-Ca}_3(\text{PO}_4)_2$  can be also written as  $\beta\text{-Ca}_{21}(\text{PO}_4)_{14}$ , and through ion substitution, many new phases with  $\beta\text{-Ca}_3(\text{PO}_4)_2$ -type structure can be constructed.<sup>2</sup> For example, when two univalent metal  $\text{M}^+$  ions are substituted for one divalent  $\text{Ca}^{2+}$  ion, the  $\beta\text{-Ca}_{20}\text{M}_2(\text{PO}_4)_{14}$  host can be obtained, namely,  $\text{Ca}_{10}\text{M}(\text{PO}_4)_7$ . Furthermore, two trivalent metal  $\text{R}^{3+}$  ions can replace three divalent  $\text{Ca}^{2+}$  ions with final composition  $\beta\text{-Ca}_{18}\text{R}_2(\text{PO}_4)_{14}$ , namely,  $\text{Ca}_9\text{R}(\text{PO}_4)_7$ . This substitution algorithm yielded a large number of new phosphors with  $\beta\text{-Ca}_3(\text{PO}_4)_2$ -type structure, such as  $\text{Ca}_{10}\text{M}(\text{PO}_4)_7:\text{Eu}^{2+}$  ( $\text{M} = \text{Li}, \text{Na}, \text{and K}$ ),<sup>8,9</sup>  $\text{Ca}_9\text{R}(\text{PO}_4)_7:\text{Eu}^{2+}$  ( $\text{R} = \text{La}, \text{Gd}, \text{Lu}, \text{and Y}$ ),<sup>10–13</sup>  $\text{Ca}_8\text{MgLn}(\text{PO}_4)_7$  ( $\text{Ln} = \text{Y}, \text{La}$ ),<sup>14,15</sup> and so on. Among these,  $\text{Ca}_{10}\text{Na}(\text{PO}_4)_7:\text{Eu}^{2+}$  phosphor gives a yellow emission centered at 550 nm,<sup>8</sup>  $\text{Ca}_9\text{Lu}(\text{PO}_4)_7:\text{Eu}^{2+}$  phosphor exhibits a broad blue-green emission band with a peak at 480 nm and  $\text{Sr}_8\text{MgY}$ -

$(\text{PO}_4)_7:\text{Eu}^{2+}$  phosphor shows yellow emission (518 nm) upon the excitation by the near-ultraviolet light in the 250–450 nm region.<sup>16</sup> Clearly, the modification of luminescence properties of phosphors is essential to fulfill the different applications in *pc*-LEDs. The photoluminescence tuning strategies mainly include ion substitution for the modification of the host composition and energy transfer among the doped rare earth ions. For example, Ji et al. revealed the  $\text{Sr}^{2+}$  ion substitution for  $\text{Ca}^{2+}$  ion in the  $\beta\text{-Ca}_3(\text{PO}_4)_2:\text{Eu}^{2+}$  induced the broad-band peak at 493–532 nm and a red shift of the emission peak located in the green-yellow region.<sup>17</sup> Moreover, the photoluminescence tuning from blue-greenish to white light and eventually to red in  $\text{Ca}_9\text{R}(\text{PO}_4)_7$  ( $\text{R} = \text{Y}$  and  $\text{Gd}$ ) can be obtained through energy transfer from  $\text{Eu}^{2+}$  to  $\text{Mn}^{2+}$  ions.<sup>11,13</sup> The emission spectra of  $\text{Ca}_{10}\text{K}(\text{PO}_4)_7:\text{Eu}^{2+}$  phosphor can be also red-shifted by increasing the  $\text{Eu}^{2+}$  concentration.<sup>9</sup>

Herein, as to the modification via substitution, the design of isostructural solid solutions and the local structure of substituted cations/anions play an important role in the photoluminescence tuning of the phosphors. Previously, the solid solutions between the nearly isostructural compounds  $\text{Sr}_3\text{AlO}_4\text{F}$  and  $\text{Sr}_3\text{SiO}_5$  have been prepared, which yields the

Received: January 2, 2017

Revised: January 19, 2017

Published: January 21, 2017

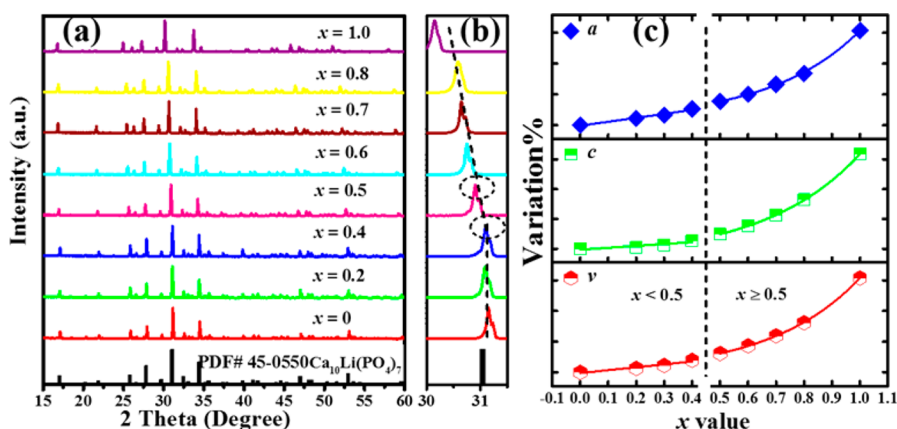


**Figure 1.** (a) XRD patterns and (b) the selected diffraction peaks near  $31^\circ$  of as-prepared  $x\text{SCP}-(1-x)\text{CLP}:0.03\text{Eu}^{2+}$  samples ( $x = 0-1.0$ ). (c) Lattice parameters  $a$  and  $c$  and the unit cell volume  $v$  of  $x\text{SCP}-(1-x)\text{CLP}:0.03\text{Eu}^{2+}$  samples as a function of  $x$ .

new green-yellow-emitting phosphor  $\text{Sr}_{2.975}\text{Ce}_{0.025}\text{Al}_{1-x}\text{Si}_x\text{O}_{4+x}\text{F}_{1-x}$  with high quantum efficiency values and high tunability in excitation and emission energy.<sup>18</sup> Except for this, the solid solutions of  $(\text{KSrPO}_4)_{1-x}(\text{BaSr})_2\text{SiO}_4)_x:\text{Eu}^{2+}$  for  $0 \leq x \leq 1$  have been designed, and the emission spectra consist of two distinct broad bands: blue ranging from 430 to 470 nm and green-yellow ranging from 515 to 570 nm.<sup>19</sup> However, no studies have been conducted on the photoluminescence tuning through the design of isostructural  $\beta\text{-Ca}_3(\text{PO}_4)_2$ -type solid solution, and this is because of the complex local structures and versatile cation sites in  $\beta\text{-Ca}_3(\text{PO}_4)_2$ -type structure for the occupation of activators.

Inspired by these reasons, we suggest herein a new solid solution  $x\text{Sr}_2\text{Ca}(\text{PO}_4)_2-(1-x)\text{Ca}_{10}\text{Li}(\text{PO}_4)_7:0.03\text{Eu}^{2+}$  (abbreviated as  $x\text{SCP}-(1-x)\text{CLP}:0.03\text{Eu}^{2+}$  hereafter) to target phosphor materials with controllable photoluminescence behavior. The local structures around the substituted cations and cation occupation rates (such as  $\text{Ca}^{2+}$ ,  $\text{Sr}^{2+}$ , and  $\text{Li}^+$ ) in each site have been investigated in detail. Therefore, depending on the variations of chemical compositions, the local environment surrounding  $\text{Eu}^{2+}$  ions changed obviously, which can lead to different luminescent properties, and the two-peak emission can further induce the photoluminescence tuning in a wide range from 414 to 515 nm. Variations of occupied rates of cations originated from structural evolution, and the structure–luminescent property relationships in  $x\text{SCP}-(1-x)\text{CLP}:0.03\text{Eu}^{2+}$  have been also studied. Moreover, temperature-dependent luminescence and two crossed excitation states in the configurational coordination diagram are performed to understand the mechanisms responsible for the quenching behavior.

## EXPERIMENTAL SECTION

**Materials and Preparation Method.**  $x\text{Sr}_2\text{Ca}(\text{PO}_4)_2-(1-x)\text{Ca}_{10}\text{Li}(\text{PO}_4)_7:0.03\text{Eu}^{2+}$  ( $0 \leq x \leq 1$ ) solid solutions were synthesized by a solid-state reaction.  $\text{CaCO}_3$  (A.R.),  $\text{SrCO}_3$  (A.R.),  $\text{Li}_2\text{CO}_3$  (A.R.),  $\text{NH}_4\text{H}_2\text{PO}_4$  (A.R.), and  $\text{Eu}_2\text{O}_3$  (99.99%) were used as raw materials. Stoichiometric amounts of the required cation sources were combined and ground together with a small amount of ethanol using an agate mortar and pestle until the mixtures were almost dry (25 min). Mixtures were then shifted to the crucible and preheated at  $800^\circ\text{C}$  for 3 h. After being ground, the powder mixtures were sintered again at  $1350^\circ\text{C}$  for 4 h under a reducing atmosphere of  $\text{N}_2\text{-H}_2$  (5%). After firing, the samples were cooled to room temperature in the furnace and were ground again.

**Characterization.** Powder X-ray diffraction (XRD) measurements were performed on a D8 Advance diffractometer (Bruker Corporation, Germany), operating at 40 kV and 35 mA with Cu K $\alpha$  radiation ( $\lambda = 1.5406 \text{ \AA}$ ). The scanning rate for phase identification was fixed at  $8^\circ \text{ min}^{-1}$  with a  $2\theta$  range from  $15^\circ$  to  $60^\circ$ , and the data for the Rietveld analysis were collected in a step-scanning mode with a step size of  $0.02^\circ$  and 5 s counting time per step over a  $2\theta$  range from  $5^\circ$  to  $120^\circ$ . Rietveld refinement was performed by using TOPAS 4.2.<sup>20</sup> High resolution transmission electron microscopic (HRTEM) images were characterized by a JEOL JEM-2010 microscope with an accelerated voltage of 200 kV. The room-temperature photoluminescence (PL) and photoluminescence excitation (PLE) spectra were carried out by a fluorescence spectrophotometer (F-4600, HITACHI, Japan) equipped with a photomultiplier tube operating at 400 V and a 150 W xenon lamp as the excitation source. The temperature dependence luminescence properties were measured FLSP9200 fluorescence spectrophotometer (Edinburgh Instruments Ltd., U.K.). The luminescence decay curves and the internal quantum efficiency were measured using the same instrument, and white  $\text{BaSO}_4$  powder was used as a reference to measure the absorption. Diffuse reflection spectra of the as-synthesized solid solution were collected at room temperature on a UV–vis–NIR spectrophotometer (SHIMADZU UV-3600) attached with an integrating sphere.

## RESULTS AND DISCUSSION

**Structural Evolution and Local Structures.** Much research has described the crystal structure of  $\beta\text{-Ca}_3(\text{PO}_4)_2$ .<sup>21</sup> There are five independent cation sites (M) in  $\beta\text{-Ca}_3(\text{PO}_4)_2$ , which are named M(1), M(2), M(3), M(4), and M(5) sites, respectively. All sites are 100% occupied by Ca ions except for M(4), and the M(4) site is only 50% occupied by the Ca ions. The  $\text{Sr}_2\text{Ca}(\text{PO}_4)_2$  phase is acquired through the substitution of  $\text{Sr}^{2+} \rightarrow \text{Ca}^{2+}$  in the  $\text{Ca}_3(\text{PO}_4)_2$  host; therefore, the host  $\text{Ca}_{10}\text{Li}(\text{PO}_4)_7$  and  $\text{Sr}_2\text{Ca}(\text{PO}_4)_2$  are isotypic and assigned to  $\beta\text{-Ca}_3(\text{PO}_4)_2$ -type structure. So we design the isostructural solid solution of  $x\text{Sr}_2\text{Ca}(\text{PO}_4)_2-(1-x)\text{Ca}_{10}\text{Li}(\text{PO}_4)_7:0.03\text{Eu}^{2+}$  in order to realize the tunable photoluminescence. The phase identification of  $x\text{SCP}-(1-x)\text{CLP}:0.03\text{Eu}^{2+}$  ( $0 \leq x \leq 1$ ) solid solutions characterized by X-ray diffraction (XRD) is shown in Figure 1a. The results indicate that all peaks of the samples can be well ascribed to a trigonal ( $R3c$ ) phase  $\text{Ca}_{10}\text{Li}(\text{PO}_4)_7$  (JCPDS card No. 45-0550), and no diffraction peaks of any other phases are detected as shown in Figure 1a. Moreover, Rietveld analysis of this series of  $x\text{SCP}-(1-x)\text{CLP}:0.03\text{Eu}^{2+}$  has been conducted, and the results also verified the phase formation of the isostructural  $\beta\text{-Ca}_3(\text{PO}_4)_2$ -type structure (Figure S1 and Table S1 in the Supporting Information).

The fine structures of the typical solid-solution composition  $0.4\text{Sr}_2\text{Ca}(\text{PO}_4)_2 \cdot 0.6\text{Ca}_{10}\text{Li}(\text{PO}_4)_7 \cdot 0.03\text{Eu}^{2+}$  sample are further examined by HRTEM as shown in Figure S2 (Supporting Information). It can be found that the continuous lattice fringe measurements with  $d$  spacing of 0.335 nm agree with the solved structure of the compound by refinement and could be assigned to the corresponding (122) plane.

Given that the ion radius of  $\text{Sr}^{2+}$  is larger than that of  $\text{Ca}^{2+}$  and  $\text{Li}^+$ , the diffraction peaks of  $x\text{SCP}-(1-x)\text{CLP} \cdot 0.03\text{Eu}^{2+}$  shift toward lower angles with respect to the position of  $\text{Ca}_{10}\text{Li}(\text{PO}_4)_7$  with the increasing of  $x$ , indicating a lattice expansion as shown in Figure 1b. Interestingly, when  $x \leq 0.4$ , the shifted range of the diffraction peaks is puny, while when  $x \geq 0.5$ , a bigger shift to lower angles can be observed. To understand this phenomenon, the detailed structural evolution and the local structures of  $\text{Ca}_{10}\text{Li}(\text{PO}_4)_7$  and  $\text{Sr}_2\text{Ca}(\text{PO}_4)_2$  are studied. Figure 2a gives the structural transformation diagram

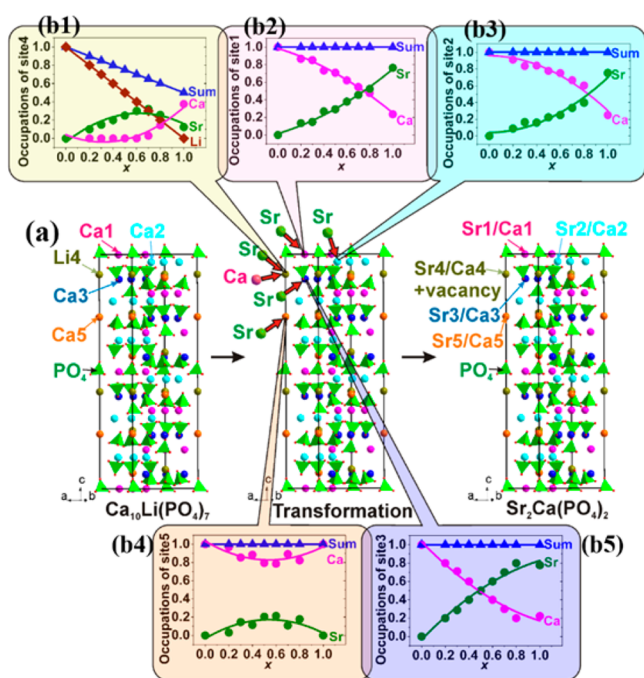


**Figure 2.** (a) Structural transformation of  $x\text{SCP}-(1-x)\text{CLP} \cdot 0.03\text{Eu}^{2+}$  ( $0 \leq x \leq 1$ ) solid solution and occupied rates of atoms (Ca, Sr, and Li) in each site (M(1), M(2), M(3), M(4), and M(5) sites) depending on the  $x$  values: (b1) M(4) site; (b2) M(1) site; (b3) M(2) site; (b4) M(5) site; and (b5) M(3) site.

from  $\text{Ca}_{10}\text{Li}(\text{PO}_4)_7$  to  $\text{Sr}_2\text{Ca}(\text{PO}_4)_2$ , and the occupation of different cations has been highlighted. For  $\text{Ca}_{10}\text{Li}(\text{PO}_4)_7$  ( $x = 0$ ), the M(1), M(2), M(3), and M(5) sites are 100% occupied by  $\text{Ca}^{2+}$  ions, and the M(4) site is 100% occupied by  $\text{Li}^+$ . However, for  $\text{Sr}_2\text{Ca}(\text{PO}_4)_2$  ( $x = 1$ ), based on the results of Rietveld refinement (Table S2, Supporting Information), the Sr ions can occupy all M sites except for M(5). It is found that the M(5) site is occupied by Sr ions with very small or near-zero concentration due to very short Ca–O bond length (2.26 Å). Furthermore, the M(4) site is only 50% occupied by  $\text{Ca}^{2+}$  and  $\text{Sr}^{2+}$  ions, and the other 50% is vacancy (□). Figure 2b1–b5 clearly presents the occupied rates of different cations ( $\text{Ca}^{2+}$ ,  $\text{Sr}^{2+}$  and  $\text{Li}^+$ ) in each site (M(1), M(2), M(3), M(4), and M(5) sites) depending on the chemical compositions,  $x$ . When the  $\text{Sr}_2\text{Ca}(\text{PO}_4)_2$  is alloyed with  $\text{Ca}_{10}\text{Li}(\text{PO}_4)_7$ , the Sr atoms will occupy all M sites of  $\text{Ca}_{10}\text{Li}(\text{PO}_4)_7$ . However, the Ca atoms will

not occupy the M(4) site, namely, the Li(4) site. Only when the introduced content of  $\text{Sr}_2\text{Ca}(\text{PO}_4)_2$  is greater than 0.5 ( $x > 0.5$ ) can the Ca atoms occupy the M(4) site. Thus, the Li(4) site is only occupied by Sr atoms if  $x \leq 0.5$ . Considering the average Li–O bond lengths (2.53 Å) in  $\text{Ca}_{10}\text{Li}(\text{PO}_4)_7$ , although the ionic radius of the Li ion is small, there is enough space to accommodate the entrance of bigger Sr atoms in the Li(4) site. When Sr atoms incorporate the Li(4) site to replace Li atoms, it enables the formation of vacancies correspondingly. One Sr atom displaces two Li atoms, and one vacancy can be obtained; such a model can be expressed as  $\text{Sr}^{2+} + \square = 2\text{Li}^+$ , as shown in Figure 3. The partial substitution of  $\text{Sr}^{2+}$  in the Li(4) site does

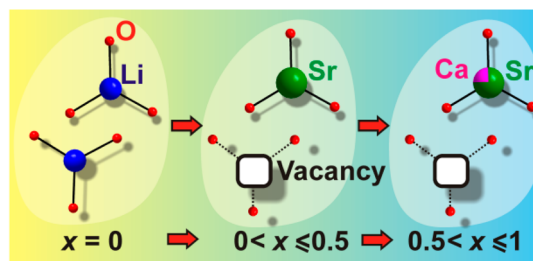


**Figure 3.** Mechanism of generating vacancies in site Li(4) through replacing  $\text{Li}^+$  ions with  $\text{Sr}^{2+}/\text{Ca}^{2+}$  ions in compound  $\text{Ca}_{10}\text{Li}(\text{PO}_4)_7$ . Different occupied conditions of Sr and Ca ions are shown.

not cause lattice expansion due to its bigger space of the Li(4) site. However, the Sr atoms will enter into M(1), M(2), and M(3) sites simultaneously to replace smaller Ca atoms, and it leads to the lattice expansion owing to the radii mismatch. The total lattice does not expand obviously, yet it is ascribed to the fact that when the Sr atoms substitute the Li atoms, the generating vacancies result in the lattice shrinkage as depicted in Figure 3. This expansion and shrinkage will offset each other, which gives rise to the lattice expansion scarcely, when the occupied content of  $\text{Sr}_2\text{Ca}(\text{PO}_4)_2$  is not enough ( $x \leq 0.4$ ). Therefore, the diffraction peaks shift toward lower angles slightly. While  $x \geq 0.5$ , the lattice shrinkage is insufficient to offset the expansion and a saltation to lower angles can be observed, as shown in the dotted circles in Figure 1b. Such variations in local structures can be also verified by the discontinuous evolution of the cell parameters and volume (Figure 1c), that is to say, the increasing range of cell parameters and volume is small at the first range ( $x \leq 0.4$ ), and afterward it becomes bigger ( $\geq 0.5$ ), which will be discussed below.

Generally, the cell parameters and volume of solid solutions increase or decrease linearly depending on the variation of the chemical compositions. For example, our group designed the solid solution of  $\text{Ca}_2(\text{Al}_{1-x}\text{Mg}_x)(\text{Al}_{1-x}\text{Si}_{1+x})\text{O}_7 \cdot \text{Eu}^{2+}$  through the chemical unit cosubstitution, and the lattice parameters present the linear variation.<sup>22</sup> However, as shown in Figure 1c, it is worth mentioning that the cell parameters ( $a$  and  $c$ ) and the total cell volume ( $V$ ) of the title solid solution increase nonlinearly with  $x$ . The crystallographic data for  $x\text{SCP}-(1-x)\text{CLP} \cdot 0.03\text{Eu}^{2+}$  are obtained from the Rietveld refinement by using the TOPAS (Table S1 in Supporting Information). It is an abnormal situation compared with previous reports. In our case, the cation substitution occurs in five sites with a complicated process, and this as-observed nonlinear behavior can be associated with vacancies. Therefore, the M(4) site has direct influence on this nonlinear variation of cell parameters, since the M(4) site is related to vacancies (Figure 3). The cell

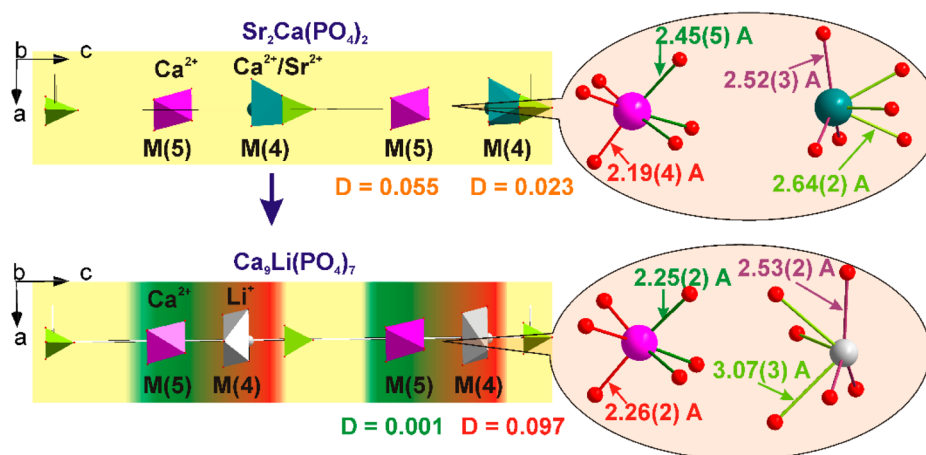


**Figure 4.** Distortion mechanism that appeared in  $x\text{SCP}-(1-x)\text{CLP}:0.03\text{Eu}^{2+}$  with decreasing  $x$ .

volume or cell parameters can be considered as a function of ion radii:

$$V(x) = k(Ax + (1-x)B) = C + Dx \quad (1)$$

where  $A$  is the ion radius of some ion which is replaced by another ion with ion radius  $B$  and  $k$  is a constant. So,  $C = kB$  and  $D = k(A - B)$ . In our case all  $\text{Li}^+$  ions are replaced by 50%  $\text{Sr}^{2+}$  and 50% vacancy, so we can rewrite

$$V(x) = k\left(Ax + (1-x)\left(\frac{B}{2} + \frac{H}{2}\right)\right) \quad (2)$$

where  $A$  is the ion radius of  $\text{Li}^+$ ,  $B$  is the ion radius of  $\text{Sr}^{2+}$ , and  $H$  is the ion radius of the vacancy. However, vacancy is not an ion, so it may have a variable value; for example, it can linearly increase or decrease as a function of  $x$ . In this case we can get  $H = H_0 + H_1x$ , and we obtain

$$V(x) = k\left(Ax + (1-x)\frac{(B + H_0 + H_1x)}{2}\right) = Ex^2 + Fx + G \quad (3)$$

where  $E = -kH_1/2$ ,  $F = kA - kB/2 - kH_0/2 + kH_1/2$ , and  $G = kB/2 + kH_0/2$ . So, we can see that the appearance of vacancy under substituting some ions can lead to a quadratic function of cell volume  $V(x) = Ex^2 + Fx + G$ . The similar dependence can be evaluated for cell parameters. Therefore, the variation of the cell parameters and volume is nonlinear.

Furthermore, we introduce the model of polyhedra distortion in order to understand the local structures of the substituted cations, especially for the M(4) site in  $x\text{SCP}-(1-x)\text{CLP}:0.03\text{Eu}^{2+}$  solid solution. The calculation of  $(\text{Ca}/\text{Sr}/\text{Li})\text{O}_n$  polyhedra distortion for the representative sites M(4) and M(5) can be realized by using the following eq 4:<sup>23,24</sup>

$$D = \frac{1}{n} \sum_{i=1}^n \frac{|l_i - l_{av}|}{l_{av}} \quad (4)$$

where  $l_i$  is the distance from the central atom to the  $i$ th coordinating atom and  $l_{av}$  is the average bond length. For M(4) and M(5) sites in SCP ( $x = 1$ ), polyhedra distortion values show a narrow range of 0.023–0.055 and a wide range of 0.001–0.097 for CLP ( $x = 0$ ). In SCP, the polyhedra distortion value for the M(4) site is minimal ( $D = 0.023$ ), while the value becomes maximal ( $D = 0.097$ ) in CLP. On the contrary, in

SCP, the polyhedra distortion value for M(5) site is maximal ( $D = 0.055$ ), and it becomes the lowest ( $D = 0.001$ ) for CLP. So we can conclude that, in the series of  $x\text{SCP}-(1-x)\text{CLP}:0.03\text{Eu}^{2+}$  solid solution, the octahedron  $\text{M}(5)\text{O}_6$  becomes more regular, but  $\text{M}(4)\text{O}_6$  becomes more distorted with decreasing  $x$  from 1 to 0. As far as M(4) and M(5) lies in one line along the  $c$ -axis, it seems that such behaviors are interconnected. Initially, in SCP both polyhedra were slightly distorted; however, with the penetration of Li in site M(4), this polyhedron  $\text{M}(4)\text{O}_6$  becomes more distorted and accumulates all distortions around itself, so  $\text{M}(5)\text{O}_6$  polyhedron releases distortion and become more regular as shown in Figure 4.

**Optical Properties.** As presented in Figure S3, the optical band gap is measured by the diffuse reflection spectra and calculated to be about 3.90 eV for  $\text{Ca}_{10}\text{Li}(\text{PO}_4)_7$ , similar to that of  $\text{Sr}_2\text{Ca}(\text{PO}_4)_2$  (3.86 eV). The band gap values indicate that they would be a suitable host for luminescent materials doped by rare earth activators. Therefore, Figure 5a gives the emission spectra of solid solution  $x\text{SCP}-(1-x)\text{CLP}:0.03\text{Eu}^{2+}$  ( $x = 0-1.0$ ) monitored at 365 nm UV excitation as a function of  $x$ . The emission band from 380 to 480 nm centered at 414 nm with a narrow bandwidth corresponds to  $\text{CLP}:0.03\text{Eu}^{2+}$  ( $x = 0$ ). Nevertheless, another emission band located at 498 nm appears with the introduction of SCP into  $\text{CLP}:0.03\text{Eu}^{2+}$ . During this cation's replacement process,  $\text{Sr}^{2+}$  ions substitute  $\text{Ca}^{2+}$  and  $\text{Li}^+$  ions as described in the above section. With the increasing of  $x$ , the emission intensity of the shorter-wavelength side at 414 nm decreases rapidly together with the gradual increase of the longer-wavelength side at about 498 nm. When  $x = 1.0$ , the emission spectra of  $\text{SCP}:0.03\text{Eu}^{2+}$  only exhibit a broad band from 420 to 680 nm centered at 515 nm. Based on such a construction of the  $\beta\text{-Ca}_3(\text{PO}_4)_2$ -type solid solution, the photoluminescence tuning has been realized. The corresponding CIE chromaticity diagram calculated from their emission spectra of  $x\text{SCP}-(1-x)\text{CLP}:0.03\text{Eu}^{2+}$  ( $x = 0-1.0$ ) phosphors and digital images upon the 365 nm UV lamp are shown in Figure 6. Furthermore, the internal quantum efficiency (IQE) of the typical sample was measured under 365 nm excitation, and the IQE value of  $x\text{SCP}-(1-x)\text{CLP}:0.03\text{Eu}^{2+}$  ( $x = 0.4$ ) is calculated to be 15.6%, which should be improved through optimization of the processing conditions.

Moreover, as shown in Figure 5a, the emission band at about 498 nm appears except for the peak at about 414 nm due to the introduction of CLP, and we proposed that such two distinct emission bands are attributed to the presence of different

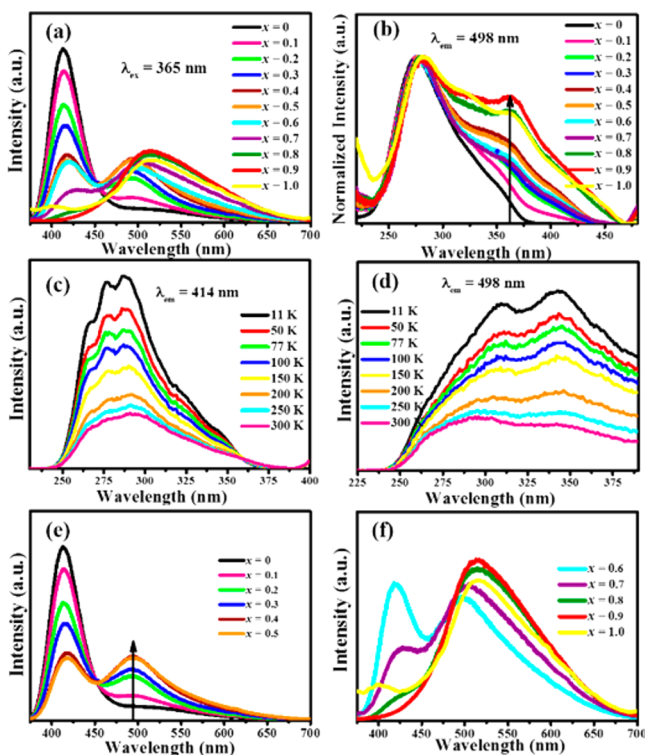


**Figure 5.** Emission spectra of  $x(\text{SCP})-(1-x)(\text{CLP}):0.03\text{Eu}^{2+}$  ( $0 \leq x \leq 1$ ) samples for different ranges: (a)  $x = 0-1.0$ , (e)  $x = 0-0.5$ , and (f)  $x = 0.6-1.0$ . (b) Normalized excitation spectra of  $x(\text{SCP})-(1-x)(\text{CLP}):0.03\text{Eu}^{2+}$  ( $0 \leq x \leq 1$ ) samples. The temperature-dependent excitation spectra of  $0.4(\text{SCP})-0.6(\text{CLP}):0.03\text{Eu}^{2+}$  for different monitored wavelengths: (c) 414 nm and (d) 498 nm.

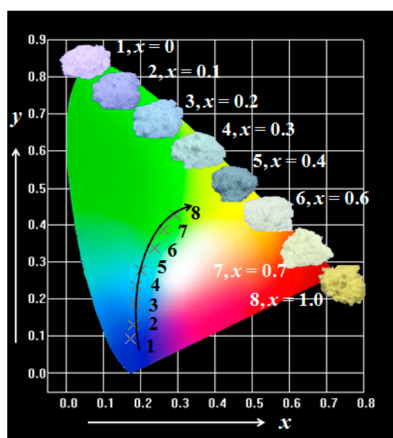


**Figure 6.** CIE chromaticity diagram and a series of digital photographs of the selected  $x\text{Sr}_2\text{Ca}(\text{PO}_4)_2-(1-x)\text{Ca}_{10}\text{Li}(\text{PO}_4)_7:0.03\text{Eu}^{2+}$  ( $x = 0, 0.1, 0.2, 0.3, 0.4, 0.6, 0.7$ , and  $1.0$ ) samples ( $\lambda_{\text{ex}} = 365$  nm).

luminescence centers, originated from  $\text{Eu}^{2+}$  occupying different cation sites. To confirm this hypothesis, the normalized excitation spectra of  $x\text{SCP}-(1-x)\text{CLP}:0.03\text{Eu}^{2+}$  ( $x = 0-1.0$ ) at room temperature are presented in Figure 5b. It can be observed that the dominant excitation band of  $\text{Eu}^{2+}$  in the  $\text{CLP}:0.03\text{Eu}^{2+}$  is located at about 276 nm in the high energy side. However, an additional excitation band centered at 363 nm in the low energy side emerges accompanied by increasing  $x$ . The appearance of both excitation bands has verified the presence of different luminescence centers. Moreover, decay behaviors of  $\text{Eu}^{2+}$  at various sites are generally different. Figure

7a presents the decay curves of  $x\text{SCP}-(1-x)\text{CLP}:0.03\text{Eu}^{2+}$  with  $x = 0, 0.2, 0.4, 0.6$ , and  $0.8$  excited at 300 nm and

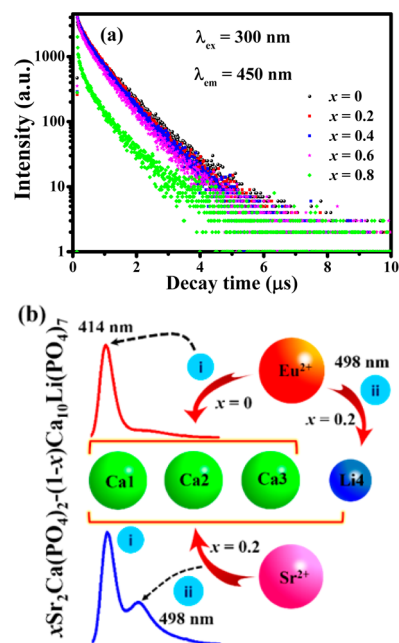


**Figure 7.** (a) Decay curves of  $\text{Eu}^{2+}$  in  $x(\text{SCP})-(1-x)(\text{CLP}):0.03\text{Eu}^{2+}$  solid solution:  $x = 0, 0.2, 0.4, 0.6$ , and  $0.8$ . (b) Specific local environment of  $\text{Eu}^{2+}$  ions in different sites and the relationship between the distribution and luminescent behavior.

monitored at 450 nm. The decay time of  $\text{Eu}^{2+}$  decreases at  $x = 0.8$  (620 ns) compared to that at  $x = 0$  (760 ns), suggesting an extra channel for the excited  $\text{Eu}^{2+}$  to depopulate,<sup>18</sup> which further proves the hypothesis for existing multiple  $\text{Eu}^{2+}$  centers in  $x\text{SCP}-(1-x)\text{CLP}$  solid solution.

There are five independent cation sites in  $x\text{SCP}-(1-x)\text{CLP}$  solid solution, and then the following questions appear: (1) which sites accommodate the dopant  $\text{Eu}^{2+}$ , and (2) which  $\text{Eu}$ -doped sites are responsible for the two emission bands? For  $\text{CLP}:\text{Eu}^{2+}$  ( $x = 0$ ), the average M–O bond length in five sites is 2.50 Å (Ca1–O), 2.49 Å (Ca2–O), 2.52 Å (Ca3–O), 2.53 Å (Li4–O), and 2.26 Å (Ca5–O) respectively, and very short Ca–O bond length (2.26 Å) in M(5) site implies that it is unsuitable for doping  $\text{Eu}^{2+}$ .<sup>18</sup> As discussed above, the M(4) site is exclusively occupied by Li. However, even if the Li–O bond length is bigger, the  $\text{Eu}^{2+}$  ions will not prefer to enter the M(4) site owing to the charge-mismatch and ion radius-mismatch. Thus,  $\text{Eu}^{2+}$  ions are potentially distributed over M(1), M(2), and M(3) sites due to no restrictions for them compared with M(4) and M(5) sites, and such a model has been demonstrated in Figure 7b. Then we suppose that the single emission band around 414 nm is originated from the three sites. With the introduction of SCP, the Sr ions can occupy all M sites except for the M(5) site due to very short Ca–O bond length (2.26 Å). Four different crystallographic sites for  $\text{Sr}^{2+}$  (and thus  $\text{Eu}^{2+}$ , a similar ion radius) are present, and two emission bands (centered at 414 and 498 nm, respectively) are found as shown in Figure 5a. In line with the above discussion, the latter emission band around 498 nm is attributed to that the  $\text{Eu}^{2+}$  ions enter the M(4) site. The specific distribution of  $\text{Eu}^{2+}$  ions in different sites and the relationship between the distribution and luminescent behavior are described in Figure 7b. To validate our speculation, the low-temperature excitation spectra

of 0.4SCP-0.6CLP:0.03Eu<sup>2+</sup> monitored at 414 and 498 nm, respectively, are provided, which reflect the intrinsic luminescence properties of the isolated Eu<sup>2+</sup> ions in  $x$ SCP-(1 -  $x$ )CLP. As depicted in Figure 5c, the excitation spectra monitored at 414 nm recorded at 14 K consist of a group of compact bands in the range of 250–350 nm, indicating that the emission band around 414 nm is originated to the Eu<sup>2+</sup> ions mainly distributed over M(1), M(2), and M(3) sites because the average bond length and coordination number of the three sites are similar, so the local environment surrounding Eu<sup>2+</sup> ions is similar. However, considering the excitation spectra monitored at 498 nm (Figure 5d), it contains two obvious excitation bands; the new peak at long wavelength (above 350 nm) is obviously different with the excitation band observed in Figure 5c, which should be assigned to the Eu<sup>2+</sup> ions that enter into the M(4) site. However, the left band in the range of 250–330 nm may be assigned to the Eu<sup>2+</sup> ions distributed over the M(1), M(2), and M(3) sites.

Turning to the influence of SCP content ( $x$ ) on the emission spectra, we found that the emission band centered at 414 nm hardly shifted with the variation of  $x$ , as given in Figure 5e,f. The emission band centered at 498 nm, for  $x$  up to 0.5, remains unchanged (no shift). Upon doping the host with higher amounts  $x > 0.5$ , a continuous red shift is observed. There are three possible causes for this redshift in the emission spectrum: centroid shift, crystal field splitting, and Stokes shift.

In the case of centroid shift, according to the model proposed by Morrison<sup>25</sup> and its modification by Dorenbos,<sup>26</sup> the centroid shift  $\epsilon_c$  (the lowering of the average of the five 5d levels) is related to the spectroscopic polarizability  $\alpha_{sp}$  of the anion. In our previous work,<sup>27,28</sup> the qualitative relationship between  $\alpha_{sp}$  and the average electronegativity of the cations  $\chi_{av}$  in Eu<sup>2+</sup>-doped compounds has been given as follows in eq 5:

$$\alpha_{sp} = 0.87 + \frac{18.76}{\chi_{av}^2} \quad (5)$$

The spectroscopic polarizability  $\alpha_{sp}$  is a negative relation with average electronegativity  $\chi_{av}$  that can be calculated by the following eq 6:<sup>28</sup>

$$\chi_{av} = \frac{1}{N_a} \sum_i^{N_c} \frac{z_i \chi_i}{\gamma} \quad (6)$$

where the summation is over all cations  $N_c$  in the formula of the compound and  $N_a$  is the number of anions in the formula. A cation of formal charge  $+z_i$  will bind on average with  $z_i/\gamma$  anions of formal charge  $-\gamma$ . The Pauling-type<sup>29</sup> electronegativity values  $\chi_i$  are from Allred.<sup>30</sup> The decreasing of average electronegativity  $\chi_{av}$  enables the spectroscopic polarizability  $\alpha_{sp}$  to enhance, which causes the centroid of the 5d excitation band to stay in a lower energy region. The corresponding redshift of the excitation band can be observed. According to eq 6, the average electronegativity  $\chi_{av}$  of cations in the  $x$ (SCP)-(1 -  $x$ ) (CLP) has been calculated as a function of  $x$  shown in Table S4 (Supporting Information). However, the values of the average electronegativity  $\chi_{av}$  nearly remain invariability, and this indicates that the centroid shift can be negligible.

In the case of crystal field splitting, based on the preceding analysis, the emission band centered at 498 nm is originated from Eu<sup>2+</sup> ions that enter into the M(4) site resulting in the appearance of a new luminescence center. As shown in Figure 3, the Ca atoms cannot enter the M(4) site to substitute Li atoms at  $x \leq 0.5$ , and until  $x > 0.5$ , the Ca atoms crowd into

M(4) site eventually. The size-mismatch of Sr and Ca atoms lead to the crystal field splitting ( $Dq$ ), and it is expressed as follows:<sup>31</sup>

$$Dq = \frac{ze^2r^4}{6R^5} \quad (7)$$

where  $Dq$  is the measurement of the crystal field strength,  $R$  is the distance between the central ion and its ligands,  $z$  is the charge or valence of the anion,  $e$  is the charge of an electron, and  $r$  is the radius of the  $d$  wave function. The ion radius of Ca<sup>2+</sup> is smaller than that of Sr<sup>2+</sup>, and the crystal field splitting becomes larger, so a red shift can be observed. These results further confirm that the emission band located at 498 nm is attributed to Eu<sup>2+</sup> ions that enter the M(4) site as shown in Figure 7b.

In the case of Stokes shift, the simplest method is to determine the Stokes shift from the energy difference between the excitation and emission maximum. According to the calculation of centroid shift and crystal field splitting, the position of the excitation band (at 363 nm) does not change at  $x \leq 0.5$  and does change at  $x > 0.5$ . This yields Stokes shifts of 7340 cm<sup>-1</sup>, 7700 cm<sup>-1</sup>, 8010 cm<sup>-1</sup>, and 8240 cm<sup>-1</sup> for  $x = 0.6$ , 0.7, 0.9, and 1.0, respectively. An increasing number indicates the Stokes shift is responsible for the red shift. Besides these, the energy transfer between luminescent centers also can lead to the red-shift of emission spectra. Actually, the presence of four crystallographic sites for Eu<sup>2+</sup>, the energy transfer between luminescent centers, cannot be excluded. The decreasing of decay time (Figure 7a) has verified an efficient energy transfer among Eu<sup>2+</sup> centers could occur. So, these results indicate that the red shift in emission spectra ( $x > 0.5$ ) is mainly caused by crystal field splitting, Stokes shift together with energy transfer.

**Thermal Quenching Properties.** Low-temperature (11–300 K) and high-temperature (300–573 K) dependent emission spectra of the selected composition of 0.4SCP-0.6CLP:0.03Eu<sup>2+</sup> ( $x = 0.4$ ) are monitored as given in Figure 8 and Figure S4. From Figure 8a and Figure S4, it is found that the emission intensity of two bands decreases significantly with rising temperature, suggesting a serious thermal quenching of

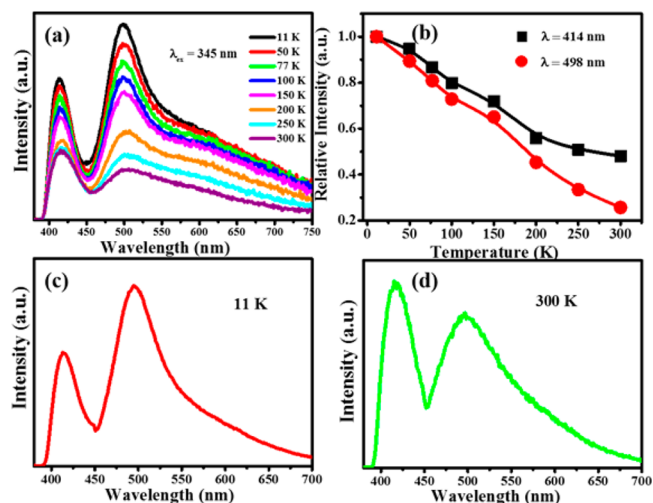


**Figure 8.** Emission spectra of the 0.4SCP-0.6CLP:0.03Eu<sup>2+</sup> sample for different temperatures: (a) 11 K–300 K, (c) 11 K, and (d) 300 K. (b) The relative emission intensity of two bands (414 and 498 nm) as a function of the temperature.

the targeted phosphor. Many reports investigated the luminescent properties of phosphor at low temperature. For instance, Meijerink et al. studied the emission spectra of YAG:Ce 0.033% at temperatures from 5 to 295 K, and the emission intensity was pretty much the same.<sup>32</sup> They also discovered the emission intensity of SrSi<sub>2</sub>O<sub>2</sub>N<sub>2</sub>:Eu<sup>2+</sup> was increasing a little from 0 to 300 K and then decreasing seriously.<sup>33</sup> Unfortunately, the emission intensity of solid solution 0.4SCP-0.6CLP:0.03Eu<sup>2+</sup> dropped sharply even if at temperatures 11–300 K. It is worth discussing and explaining this phenomenon.

On the basis of a previous report, the temperature dependence of the integrated emission intensity of luminescent materials is usually described through eq 8:<sup>34</sup>

$$I(T) \approx \frac{I_0}{1 + c \exp\left(-\frac{\Delta E}{kT}\right)} \quad (8)$$

where  $I_0$  is the initial intensity at low temperatures and  $I(T)$  is the intensity at a given temperature  $T$  (K).  $\Delta E$  is the activation energy,  $c$  is a constant, and  $k$  is the Boltzmann constant ( $8.62 \times 10^{-5}$  eV). The integrated emission intensities of two bands (414 and 498 nm) are plotted respectively as a function of temperature in Figure 9a,b. The lines through the data points

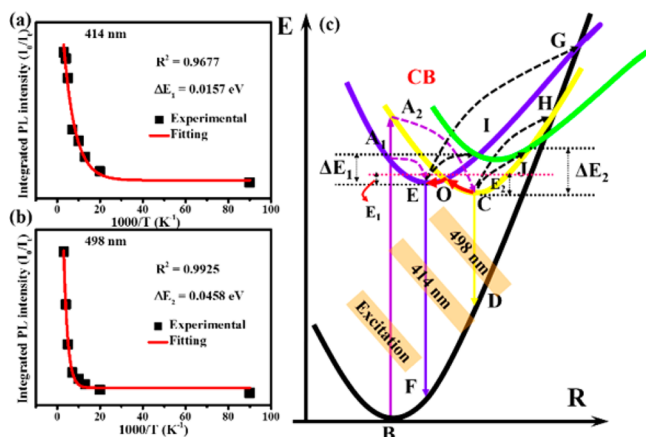


**Figure 9.** Activation energy ( $\Delta E$ ) for thermal quenching of (a) peak-414 nm and (b) peak-498 nm in 0.4SCP-0.6CLP:0.03Eu<sup>2+</sup>. (c) Configurational coordinated diagram of Eu<sup>2+</sup> in  $x$ SCP-(1-x)CLP solid solution.

represent a fit according to eq 8. The calculated  $\Delta E_1$  and  $\Delta E_2$  for the 414 and 498 nm bands are 0.0157 eV and 0.0458 eV, respectively, which is very small. Generally, two possible reasons, Stokes shift and photoionization process, are responsible for the thermal quenching behavior of luminescent materials. As depicted previously, the excitation and emission spectra of 0.4SCP-0.6CLP:0.03Eu<sup>2+</sup> hardly shift compared to that of CLP:0.03Eu<sup>2+</sup> shown in Figure 5a,b. Hence, the Stokes shift should not be a major reason. On the basis of the above results, this thermal quenching behavior should be associated with the photoionization process.

To better understand the thermal quenching behavior of the targeted phosphors, the configurational coordinated diagram of Eu<sup>2+</sup> in the 0.4SCP-0.6CLP solid solution is adopted.  $\Delta E$  is the activation energy connected with this process (the energy gap between the lowest energy Eu<sup>2+</sup> 4f<sup>6</sup>5d<sup>1</sup>-excited level and the bottom of the conduction band).<sup>33</sup> According to the calculated activation energy  $\Delta E_1$ -414 nm and  $\Delta E_2$ -498 nm, the lowest

energy Eu<sup>2+</sup> 4f<sup>6</sup>5d<sup>1</sup>-excited level is extremely close to the conduction band (CB), which will result in a photoionization process, even at low temperatures (11–300 K).<sup>35</sup> The configurational coordinated diagram of Eu<sup>2+</sup> in  $x$ SCP-(1-x)CLP solid solution is depicted at Figure 9c, and following the 365 nm excitation, the electrons first relax to the equilibrium configuration of the 5d excited states (lines A<sub>1</sub>B and A<sub>2</sub>B) through vibrational relaxation, then return to the 4f ground state through radiative transition (lines EF and CD), and emit 414 nm (blue line) and 498 nm (yellow line). Nevertheless, the energy difference between 5d levels and the conduction band is small, and the electrons will be thermally activated to the conduction band (through process EI and CJ) rather than returning to the ground state; this is the photoionization process. The nonradiative transition (process EG and CH) from the excited state to the ground state can also take place through the crossing point at high temperatures, but the influence of nonradiative transition is negligible compared with the photoionization process. Furthermore, with regard to two emission bands, the decay rates of emission intensity are not consistent as shown in Figure 8b. The emission intensity of the low-energy side is stronger than that of high-energy side at 11 K, while with the temperature raised to 300 K, the emission intensity of the high-energy side is relatively higher even if the emission intensities of both peaks are decreasing as shown in Figure 8c,d. To explain this observation, it should be considered that thermally active phonon-assisted tunneling, from the excited states of the low-energy emission side to the excited states of the high-energy emission side, can occur in the configuration coordinate diagram.<sup>36</sup> At lower temperature, the barrier E1 can be overcome, and the excited electrons of the high-energy side will transfer to the excited state of the low-energy side through crossing point O; thus, the low-energy emission is dominant. As the temperature subsequently rises, thermal activation causes the electrons to cross the point of intersection of the yellow and blue curves, the electronic back-transfer over the barrier E2 is possible, and the higher energy emission is dominant correspondingly.<sup>37</sup> This model successfully explains why the thermal stability of the solid solution 0.4SCP-0.6CLP:0.03Eu<sup>2+</sup> is not good, why the intensity of 498 nm declines as the temperature increases from 11 to 300 K, and why the intensity of the 414 nm line increases.

## CONCLUSIONS

In summary, we designed and prepared the new  $\beta$ -Ca<sub>3</sub>(PO<sub>4</sub>)<sub>2</sub>-type solid solution phosphors of  $x$ Sr<sub>2</sub>Ca(PO<sub>4</sub>)<sub>2</sub>-(1-x)-Ca<sub>10</sub>Li(PO<sub>4</sub>)<sub>7</sub>:0.03Eu<sup>2+</sup> with controllable photoluminescence properties. Depending on the variations of the chemical compositions  $x$  up to 1, the vacancies from the M(4) site appear and enable a nonlinear variation of cell parameters and volume, and the polyhedron M(4)O<sub>6</sub> also becomes more distorted, while M(5)O<sub>6</sub> polyhedron releases distortion and becomes more regular. Therefore, a different local environment surrounding Eu<sup>2+</sup> ions leads to the two-peak emission behavior, and the emission band around 414 nm is ascribed to Eu<sup>2+</sup> ions that are distributed over M(1), M(2), and M(3) sites, while the emission band around 498 nm is attributed to the Eu<sup>2+</sup> ions that enter the M(4) site. The emission peaks at about 498 nm of  $x$ SCP-(1-x)CLP:Eu<sup>2+</sup> keep invariable at  $x \leq 0.5$ , and it shows a red shift at  $x > 0.5$  with increasing  $x$  values; such red shift behavior can be assigned to the combined effect of the crystal field splitting, Stokes shift, and energy transfer among Eu<sup>2+</sup> ions. Temperature-dependent luminescence measurement

is also performed to understand the mechanism responsible for the quenching behavior, which is that the  $\text{Eu}^{2+} 4f^6 5d^1$ -excited level is extremely close to the conduction band resulting in the photoionization process, and the two crossed excitation states in the configurational coordination diagram are proposed to explain the intensity of the emission band (414 nm) that increased with temperature (11–300 K). It is shown that local structures allow predictive control of photoluminescence tuning and therefore provide a new method of phosphor development.

## ■ ASSOCIATED CONTENT

### Supporting Information

The Supporting Information is available free of charge on the ACS Publications website at DOI: 10.1021/acs.chemmater.7b00006.

Rietveld refinements, HRTEM, diffuse reflectance spectra, and high-temperature (300–573 K) dependent emission spectra for Figures S1–S4; structural data and average electronegativity for Tables S1–S4 (PDF)

## ■ AUTHOR INFORMATION

### Corresponding Author

\*E-mail: xiazg@ustb.edu.cn (Z. Xia).

### ORCID

Zhiguo Xia: 0000-0002-9670-3223

### Notes

The authors declare no competing financial interest.

## ■ ACKNOWLEDGMENTS

The present work was supported by the National Natural Science Foundation of China (Grants 91622125 and 51572023), Natural Science Foundations of Beijing (2172036), and Fundamental Research Funds for the Central Universities (FRF-TP-15-003A2).

## ■ REFERENCES

- Xia, Z. G.; Liu, Q. L. Progress in Discovery and Structural Design of Color Conversion Phosphors for LEDs. *Prog. Mater. Sci.* **2016**, *84*, 59–117.
- Xia, Z. G.; Liu, G. K.; Wen, J. G.; Mei, Z. G.; Balasubramanian, M.; Molokeev, M. S.; Peng, L. C.; Gu, L.; Miller, D. J.; Liu, Q. L.; Poeppelmeier, K. R. Tuning of Photoluminescence by Cation Nanosegregation in the  $(\text{CaMg})_x(\text{NaSc})_{(1-x)}\text{Si}_2\text{O}_6$  Solid Solution. *J. Am. Chem. Soc.* **2016**, *138*, 1158–1161.
- Peng, M. Y.; Yin, X. W.; Tanner, P. A.; Brik, M. G.; Li, P. F. Site Occupancy Preference, Enhancement Mechanism, and Thermal Resistance of  $\text{Mn}^{4+}$  Red Luminescence in  $\text{Sr}_4\text{Al}_{14}\text{O}_{25}$ :  $\text{Mn}^{4+}$  for Warm WLEDs. *Chem. Mater.* **2015**, *27*, 2938–2945.
- Wagatha, P.; Pust, P.; Weiler, V.; Wochnik, A. S.; Schmidt, P. J.; Scheu, C.; Schnick, W.  $\text{Ca}_{18.75}\text{Li}_{10.5}[\text{Al}_{39}\text{N}_{55}]:\text{Eu}^{2+}$  Supertetrahedron Phosphor for Solid-State Lighting. *Chem. Mater.* **2016**, *28*, 1220–1226.
- Huang, L.; Zhu, Y. W.; Zhang, X. J.; Zou, R.; Pan, F. J.; Wang, J.; Wu, M. M. HF-Free Hydrothermal Route for Synthesis of Highly Efficient Narrow-Band Red Emitting Phosphor  $\text{K}_2\text{Si}_{1-x}\text{F}_6:\text{xMn}^{4+}$  for Warm White Light-Emitting Diodes. *Chem. Mater.* **2016**, *28*, 1495–1502.
- Xia, Z. G.; Liu, H. K.; Li, X.; Liu, C. Y. Identification of the Crystallographic Sites of  $\text{Eu}^{2+}$  in  $\text{Ca}_9\text{NaMg}(\text{PO}_4)_7$ : Structure and Luminescence Properties Study. *Dalton Trans.* **2013**, *42*, 16588–16595.
- Ji, H. P.; Huang, Z. H.; Xia, Z. G.; Molokeev, M. S.; Atuchin, V. V.; Fang, M. H.; Liu, Y. G. Discovery of New Solid Solution Phosphors via Cation Substitution-Dependent Phase Transition in

$\text{M}_3(\text{PO}_4)_2:\text{Eu}^{2+}$  ( $\text{M} = \text{Ca}/\text{Sr}/\text{Ba}$ ) Quasi-Binary Sets. *J. Phys. Chem. C* **2015**, *119*, 2038–2045.

(8) Yu, H.; Deng, D. G.; Li, Y. Q.; Xu, S. Q.; Li, Y. Y.; Yu, C. P.; Ding, Y. Y.; Lu, H. W.; Yin, H. Y.; Nie, Q. L. Electronic Structure and Photoluminescence Properties of Yellow-emitting  $\text{Ca}_{10}\text{Na}(\text{PO}_4)_7:\text{Eu}^{2+}$  Phosphor for White light-emitting diodes. *J. Lumin.* **2013**, *143*, 132–136.

(9) Liu, W. R.; Chiu, Y. C.; Yeh, Y. T.; Jang, S. M.; Chen, T. M. Luminescence and Energy Transfer Mechanism in  $\text{Ca}_{10}\text{K}(\text{PO}_4)_7:\text{Eu}^{2+}, \text{Mn}^{2+}$  phosphor. *J. Electrochem. Soc.* **2009**, *156*, J165–J169.

(10) Huang, C. H.; Chen, T. M.  $\text{Ca}_9\text{La}(\text{PO}_4)_7:\text{Eu}^{2+}, \text{Mn}^{2+}$ : an Emission-tunable Phosphor through Efficient Energy Transfer for White Light-emitting Diodes. *Opt. Express* **2010**, *18*, 5089–5099.

(11) Guo, N.; You, H. P.; Song, Y. H.; Yang, M.; Liu, K.; Zheng, Y. H.; Huang, Y. J.; Zhang, H. J. White-light Emission from a single-emitting-component  $\text{Ca}_9\text{Gd}(\text{PO}_4)_7:\text{Eu}^{2+}, \text{Mn}^{2+}$  Phosphor with Tunable Luminescent Properties for Near-UV Light-emitting Diodes. *J. Mater. Chem.* **2010**, *20*, 9061–9067.

(12) Guo, N.; Huang, Y. J.; You, H. P.; Yang, M.; Song, Y. H.; Liu, K.; Zheng, Y. H.  $\text{Ca}_9\text{Lu}(\text{PO}_4)_7:\text{Eu}^{2+}, \text{Mn}^{2+}$ : A Potential Single-phased White-Light-emitting Phosphor Suitable for White-light-emitting Diodes. *Inorg. Chem.* **2010**, *49*, 10907–10913.

(13) Huang, C. H.; Chen, T. M.; Liu, W. R.; Chiu, Y. C.; Yeh, Y. T.; Jang, S. M. A Single-phased Emission-tunable Phosphor  $\text{Ca}_9\text{Y}(\text{PO}_4)_7:\text{Eu}^{2+}, \text{Mn}^{2+}$  with Efficient Energy Transfer for White-light-emitting Diodes. *ACS Appl. Mater. Interfaces* **2010**, *2*, 259–264.

(14) Wen, D. W.; Dong, Z. Y.; Shi, J. X.; Gong, M. L.; Wu, M. M. Standard White-emitting  $\text{Ca}_8\text{MgY}(\text{PO}_4)_7:\text{Eu}^{2+}, \text{Mn}^{2+}$  Phosphor for White-light-emitting LEDs. *ECS J. Solid State Sci. Technol.* **2013**, *2*, R178–R185.

(15) Xue, Y. N.; Xiao, F.; Zhang, Q. Y. A Red-emitting  $\text{Ca}_8\text{MgLa}(\text{PO}_4)_7:\text{Ce}^{3+}, \text{Mn}^{2+}$  Phosphor for UV-based White LEDs Application. *Spectrochim. Acta, Part A* **2011**, *78*, 1445–1448.

(16) Huang, C. H.; Chen, T. M. Novel Yellow-emitting  $\text{Sr}_8\text{MgLn}(\text{PO}_4)_7:\text{Eu}^{2+}$  ( $\text{Ln} = \text{Y}, \text{La}$ ) Phosphors for Applications in White LEDs with Excellent Color Rendering Index. *Inorg. Chem.* **2011**, *50*, 5725–5730.

(17) Ji, H. P.; Huang, Z. H.; Xia, Z. G.; Molokeev, M. S.; Atuchin, V. V.; Huang, S. F. Cation Substitution Dependent Bimodal Photoluminescence in Whitlockite Structural  $\text{Ca}_{3-x}\text{Sr}_x(\text{PO}_4)_2:\text{Eu}^{2+}$  ( $0 \leq x \leq 2$ ) Solid Solution Phosphors. *Inorg. Chem.* **2014**, *53*, 11119–11124.

(18) Im, W. B.; George, N.; Kurzman, J.; Brinkley, S.; Mikhailovsky, A.; Hu, J.; Chmelka, B. F.; DenBaars, S. P.; Seshadri, R. Efficient and Color-Tunable Oxyfluoride Solid Solution Phosphors for Solid-State White Lighting. *Adv. Mater.* **2011**, *23* (20), 2300–2305.

(19) Han, J. K.; Hannah, M. E.; Piquette, A.; Talbot, J. B.; Mishra, K. C.; McKittrick, J. Europium-Activated  $\text{KSrPO}_4-(\text{Ba},\text{Sr})_2\text{SiO}_4$  Solid Solutions as Color-tunable Phosphors for Near-UV Light-emitting Diode Applications. *J. Am. Ceram. Soc.* **2013**, *96*, 1526–1532.

(20) TOPAS, version 4: General Profile and Structure Analysis Software for Powder Diffraction Data—User's Manual; Bruker AXS: Karlsruhe, Germany, 2008.

(21) Han, J.; Zhou, W. L.; Qiu, Z. X.; Yu, L. P.; Zhang, J. L.; Xie, Q. J.; Wang, J.; Lian, S. X. Redistribution of Activator Tuning of Photoluminescence by Isovalent and Aliovalent Cation Substitutions in Whitlockite Phosphors. *J. Phys. Chem. C* **2015**, *119*, 16853–16859.

(22) Xia, Z. G.; Ma, C. G.; Molokeev, M. S.; Liu, Q. L.; Rickert, K.; Poeppelmeier, K. R. Chemical Unit Cosubstitution and Tuning of Photoluminescence in the  $\text{Ca}_2(\text{Al}_{1-x}\text{Mg}_x)(\text{Al}_{1-x}\text{Si}_{1+x})\text{O}_7:\text{Eu}^{2+}$  Phosphor. *J. Am. Chem. Soc.* **2015**, *137*, 12494–12497.

(23) Baur, W. The Geometry of Polyhedral Distortions. Predictive Relationships for the Phosphate group. *Acta Crystallogr., Sect. B: Struct. Crystallogr. Cryst. Chem.* **1974**, *30* (5), 1195–1215.

(24) Miao, S. H.; Xia, Z. G.; Molokeev, M. S.; Chen, M. Y.; Zhang, J.; Liu, Q. L. Effect of Al/Si Substitution on the Structure and Luminescence Properties of  $\text{CaSrSiO}_4:\text{Ce}^{3+}$  Phosphors: Analysis Based on the Polyhedra Distortion. *J. Mater. Chem. C* **2015**, *3*, 4616–4622.

- (25) Morrison, C. A. Host Dependence of the Rare-earth ion Energy Separation  $4f^{N-4f^{N-1}}n_l$ . *J. Chem. Phys.* **1980**, *72*, 1001–1002.
- (26) Dorenbos, P. 5d-level Energies of  $\text{Ce}^{3+}$  and the Crystalline Environment. I. Fluoride Compounds. *Phys. Rev. B: Condens. Matter Mater. Phys.* **2000**, *62*, 15640.
- (27) Wang, T.; Xia, Z. G.; Xiang, Q. C.; Qin, S. Q.; Liu, Q. L. Relationship of 5d-level Energies of  $\text{Ce}^{3+}$  with the Structure and Composition of Nitride Hosts. *J. Lumin.* **2015**, *166*, 106–110.
- (28) Wang, T.; Xiang, Q. C.; Xia, Z. G.; Chen, J.; Liu, Q. L. Evolution of Structure and Photoluminescence by Cation Cosubstitution in  $\text{Eu}^{2+}$ -Doped  $(\text{Ca}_{1-x}\text{Li}_x)(\text{Al}_{1-x}\text{Si}_{1+x})\text{N}_3$  Solid Solutions. *Inorg. Chem.* **2016**, *55* (6), 2929–2933.
- (29) Pauling, L. *The nature of the chemical bond and the structure of molecules and crystals: an introduction to modern structural chemistry*; Cornell University Press: 1960; Vol. 18.
- (30) Allred, A. Electronegativity Values from Thermochemical Data. *J. Inorg. Nucl. Chem.* **1961**, *17*, 215–221.
- (31) Duan, C.; Reid, M. A Simple Model for  $f \rightarrow d$  Transitions of Rare-earth Ions in Crystals. *J. Solid State Chem.* **2003**, *171*, 299–303.
- (32) Bachmann, V.; Ronda, C.; Meijerink, A. Temperature Quenching of Yellow  $\text{Ce}^{3+}$  Luminescence in YAG: Ce. *Chem. Mater.* **2009**, *21*, 2077–2084.
- (33) Bachmann, V.; Ronda, C.; Oeckler, O.; Schnick, W.; Meijerink, A. Color Point Tuning for  $(\text{Sr}, \text{Ca}, \text{Ba})\text{Si}_2\text{O}_2\text{N}_2$ :  $\text{Eu}^{2+}$  for White Light LEDs. *Chem. Mater.* **2009**, *21*, 316–325.
- (34) Bhushan, S.; Chukichev, M. Temperature Dependent Studies of Cathodoluminescence of Green Band of ZnO Crystals. *J. Mater. Sci. Lett.* **1988**, *7*, 319–321.
- (35) Zhu, Q. Q.; Wang, L.; Hirosaki, N.; Hao, L. Y.; Xu, X.; Xie, R. J. Extra-Broad Band Orange-Emitting  $\text{Ce}^{3+}$ -Doped  $\text{Y}_3\text{Si}_5\text{N}_9\text{O}$  Phosphor for Solid-State Lighting: Electronic, Crystal Structures and Luminescence Properties. *Chem. Mater.* **2016**, *28*, 4829–4839.
- (36) Shionoya, S.; Yen, W. M.; Yamamoto, H. *Phosphor handbook*; CRC Press: 2006.
- (37) Kim, J. S.; Park, Y. H.; Kim, S. M.; Choi, J. C.; Park, H. L. Temperature-dependent Emission Spectra of  $\text{M}_2\text{SiO}_4:\text{Eu}^{2+}$  ( $\text{M} = \text{Ca}, \text{Sr}, \text{Ba}$ ) Phosphors for Green and Greenish White LEDs. *Solid State Commun.* **2005**, *133*, 445–448.